

Carbon dioxide adsorption and conversion to methane and ethane on hydrogen boride sheets

Taiga Goto¹, Shin-ichi Ito ^{2,3}, Satish Laxman Shinde³, Ryota Ishibiki¹, Yasuyuki Hikita⁴, Iwao Matsuda ⁵, Ikutaro Hamada ⁶✉, Hideo Hosono ^{2,7} & Takahiro Kondo ^{2,3}✉

Hydrogen boride (HB) sheets are metal-free two-dimensional materials comprising boron and hydrogen in a 1:1 stoichiometric ratio. In spite of the several advancements, the fundamental interactions between HB sheets and discrete molecules remain unclear. Here, we report the adsorption of CO₂ and its conversion to CH₄ and C₂H₆ using hydrogen-deficient HB sheets. Although fresh HB sheets did not adsorb CO₂, hydrogen-deficient HB sheets reproducibly physisorbed CO₂ at 297 K. The adsorption followed the Langmuir model with a saturation coverage of 2.4×10^{-4} mol g⁻¹ and a heat of adsorption of approximately 20 kJ mol⁻¹, which was supported by density functional theory calculations. When heated in a CO₂ atmosphere, hydrogen-deficient HB began reacting with CO₂ at 423 K. The detection of CH₄ and C₂H₆ as CO₂ reaction products in a moist atmosphere indicated that hydrogen-deficient HB promotes C-C coupling and CO₂ conversion reactions. Our findings highlight the application potential of HB sheets as catalysts for CO₂ conversion.

¹Graduate School of Pure and Applied Sciences, University of Tsukuba, 1-1-1, Tennodai, Tsukuba 305-8573, Japan. ²Materials Research Center for Element Strategy, Tokyo Institute of Technology, Yokohama 226-8503, Japan. ³Department of Materials Science and Tsukuba Research Center for Energy Materials Science, Faculty of Pure and Applied Sciences, University of Tsukuba, Tsukuba 305-8573, Japan. ⁴Advanced Research and Innovation Center, DENSO CORPORATION, Nisshin, Aichi 470-0111, Japan. ⁵Institute for Solid State Physics (ISSP), The University of Tokyo, Kashiwa, Chiba 277-8581, Japan. ⁶Department of Precision Engineering, Graduate School of Engineering, Osaka University, 2-1 Yamada-oka, Suita, Osaka 565-0871, Japan. ⁷International Center for Materials Nanoarchitectonics, National Institute for Materials Science, Tsukuba 305-0044, Japan. ✉email: ihamada@prec.eng.osaka-u.ac.jp; takahiro@ims.tsukuba.ac.jp

Two-dimensional (2D) materials have been applied in various fields, including catalysis and electronics, because of their large surface areas and advantageous electronic states^{1–6}. We previously reported hydrogen boride (HB) sheets comprising boron and hydrogen in a 1:1 stoichiometric ratio as a 2D metal-free material that can be formed via ion-exchange reactions between the protons and magnesium cations in magnesium diboride following an exfoliation process⁷. Boron atoms form a hexagonal 2D network in the HB sheets, wherein hydrogen atoms are bound to boron atoms by 3-center-2-electron (B–H–B) and 2-center-2-electron (B–H) bonds⁸. HB sheets have been experimentally verified to exhibit excellent solid acid catalytic activity^{9,10}, specific metal ion reducibility^{11,12}, semimetal electronic properties¹³, highly-sensitive gas-sensor applicability⁸, and light-responsive hydrogen release¹⁴. Furthermore, theoretical studies have revealed the intriguing electronic¹⁵, optical, and thermal properties^{16,17} of HB sheets, as well as their possible applications in rechargeable Li/Na ion battery electrodes^{18,19}, hydrogen release devices^{20,21}, reversible hydrogen storage²², current limiters²³, photodetectors²³, individual amino acid sensors²⁴, and anodes for rechargeable potassium-ion batteries with high capacities, low voltages, and high rate-performance²⁵. Furthermore, the formation of HB sheets paves the way for the conceptual development of new types of HB materials^{26–32}. In spite of the aforementioned advancements, the fundamental interactions between HB sheets and discrete molecules remain unclear.

In this work, we focus on the interaction between CO₂ and HB sheets because boron is a key element associated with the activation of CO₂ in organic chemistry^{33,34}. Elemental boron has also been reported to facilitate the reduction of CO₂ under light irradiation³⁵. Theoretical calculations have indicated that CO₂ capture on solid boron clusters is kinetically and thermodynamically feasible³⁶, and that planar-type boron clusters can capture CO₂³⁷ and separate it from N₂ and CH₄³⁸. Theoretical predictions have also indicated that 2D-planar boron (borophene) shows promise as a material for switchable charge-modulated CO₂ capture^{39,40} and as an electrocatalyst for the conversion of CO₂ to CH₄⁴¹. B₄₀ fullerene has been predicted to be an efficient material for CO₂ capture, storage, and separation based on theoretical calculations^{42,43}. Theoretical studies have also highlighted the potential of B₈₀ fullerene as a metal-free photocatalyst for the efficient conversion of CO₂ to HCOOH⁴⁴, as well as CO₂ capture and separation applications⁴⁵. Borohydrides are widely used as reducing agents in chemical synthetic processes, as hydrogen storage materials in emerging energy applications, and as reagents for the reduction of CO₂^{46–50}. Boron nitride, boron sulfide, and boron phosphide have also been reported to be efficient metal-free catalysts for converting CO₂ into valuable fuels^{51–55}.

In this study, we experimentally and theoretically investigated the adsorption characteristics of CO₂ molecules on HB sheets, and verified their utilization prospects as CO₂ conversion catalysts. To investigate the effect of pre-treatment temperature, the HB sheets were pre-treated in vacuum for 1 h at four different temperatures (323, 473, 523, and 573 K), with the resultant samples denoted as HB-323K, HB-473K, HB-523K, and HB-573K, respectively. Further, we experimentally confirmed the formation of CH₄ and C₂H₆ through the thermal reaction between hydrogen-deficient HB sheets and CO₂ in a moist atmosphere, which indicates that hydrogen-deficient HB promotes C–C coupling in addition to CO₂ conversion.

Results and discussion

CO₂ adsorption on HB sheets. The rate of adsorption of CO₂ on the HB sheets was determined by measuring the change in

pressure following the introduction of CO₂ into a vacuum chamber (base pressure lower than 10^{–6} Torr) containing HB sheets (30–50 mg). Typical results at 297 K and a CO₂ pressure of 15 Torr are shown in Fig. 1a. For the HB-323K sample (blue triangles), the CO₂ pressure remained unchanged with time, indicating that CO₂ does not adsorb onto HB sheets pre-treated at 323 K. However, for the HB-473K sample (red circles), the CO₂ pressure decreased with time until reaching a constant value, indicating that CO₂ was successfully adsorbed on the HB-473K sample and attained adsorption/desorption equilibrium at 297 K. The HB-473K sample became hydrogen-deficient compared to pristine HB because a sub-stoichiometric fraction of hydrogen was released as H₂ gas via thermal decomposition. The results in Fig. 1a illustrate the adsorption of CO₂ when the HB sheets became hydrogen-deficient. Based on gas chromatography analysis and our previous results employing thermal desorption spectroscopy^{7,9}, the fraction of hydrogen remaining in the HB-473K sample (x in H_{*x*}B₁) was estimated to be 0.81 < x < 0.95. The variation of x originates from the differences in the hydrogen content between samples⁷ as well as errors in temperature measurement.

The amount of adsorbed CO₂, n_{ads} , was estimated from the pressure drop (ΔP) in Fig. 1a using the ideal gas law:

$$n_{\text{ads}} = \frac{\Delta PV}{RT},$$

where V is the volume of the experimental cell, R is the ideal gas constant, and T is the temperature (297 K). We used the ideal gas law instead of the van der Waals equation because the effects of the intermolecular interactions and the volume occupied by the gas molecules were small and within the uncertainty of our experiment. The amount of CO₂ adsorbed on HB-473K was plotted as a function of CO₂ pressure at different sample temperatures (253–323 K) to construct the adsorption isotherms shown in Fig. 1b (also see Supplementary Fig. 1). In each case, the amount of CO₂ adsorbed increased with increasing CO₂ pressure and decreasing temperature. This behavior is consistent with type-I Langmuir adsorption according to the International Union of Pure and Applied Chemistry (IUPAC) classification. This indicates that the adsorption site and adsorption energy are independent of the amount of CO₂ adsorbed.

To characterize the type of adsorption, a P/n_{ads} vs P plot was constructed (Fig. 1c) using the results obtained in Fig. 1b at CO₂ pressures (P) of up to 400 Torr at 273 K. The linear relationship between P/n_{ads} and P clearly indicated that the adsorption of CO₂ on the HB-473K sample followed a type-I Langmuir isotherm curve. The slight deviation in the low-pressure region was attributed to the small number of CO₂ chemisorption sites on HB-473K. Specifically, 1.44×10^{-5} mol g_{HB}^{–1} of CO₂ was considered to be chemisorbed (Supplementary Fig. 2), whereas the majority of the CO₂, as modeled by the type-I isotherm, remained in the physisorbed state (as discussed below). From the slope in Fig. 1c, the amount of CO₂ adsorbed at saturation (n_s) and the equilibrium constant (K) were estimated as $n_s = 2.43 \times 10^{-4}$ mol g_{HB}^{–1} and $K = 0.011$ using the following relationship:

$$\frac{P}{V} = \frac{P}{n_s} + \frac{1}{Kn_s}$$

The estimated n_s corresponded to $7.8 \pm 6.3\%$ of the H-vacant sites in HB-473K (H_{*x*}B₁, 0.81 < x < 0.95). In this calculation, we neglected the influence of the morphological characteristics of the HB sheet including sheet stacking, and assumed that all atoms in the sheets were exposed to the gas. Therefore, the estimated percentage was within a lower limit. The estimated coverage suggests that only some of the hydrogen-deficient sites in HB-473K act as adsorption sites for CO₂.

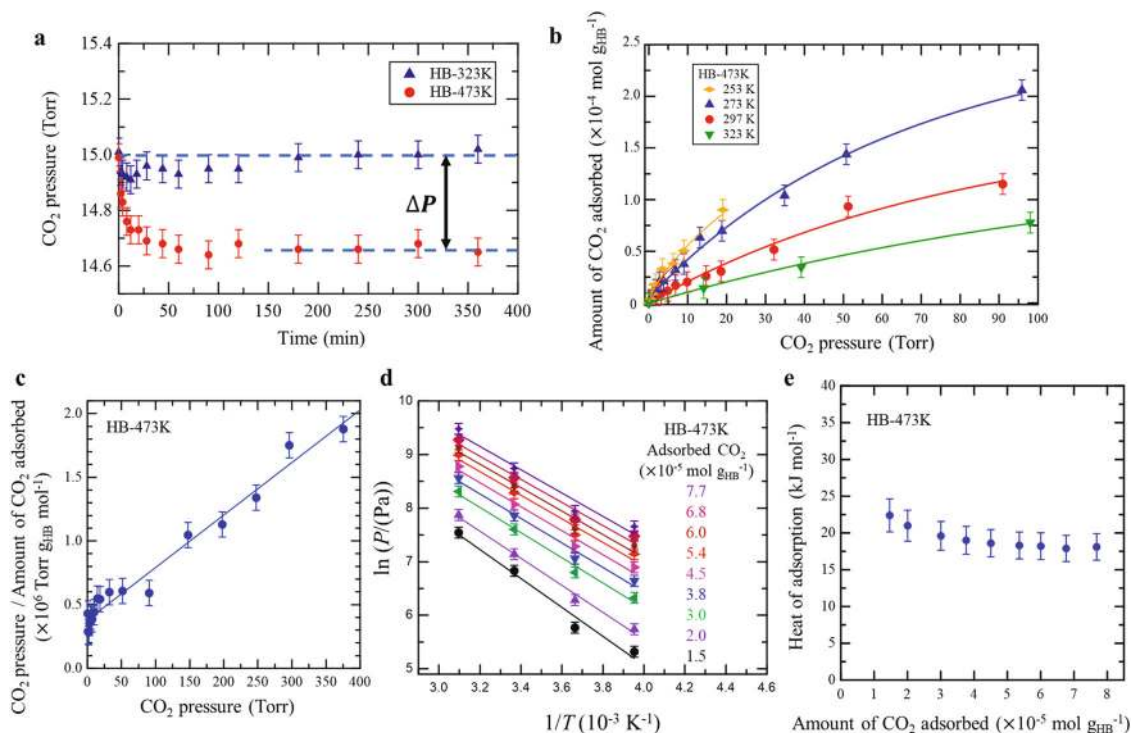


Fig. 1 CO₂ adsorption on hydrogen boride (HB) sheets. **a** Change in pressure of CO₂ with time following exposure to HB sheets at 297 K. Blue triangles: HB sheets preheated at 323 K for 1 h in vacuum (HB-323K). Red circles: HB sheets preheated at 473 K for 1 h in vacuum (HB-473K), at which temperature the HB sheets became hydrogen-deficient (H_xB₁, 0.81 < x < 0.95) due to partial decomposition and hydrogen release (see the text for details). **b** Isotherms of CO₂ adsorption on HB-473K. **c** P/n_{ads} vs P plot for the results in **b** at 273 K and the results obtained at higher CO₂ pressures (P) of up to 400 Torr (n_{ads} denotes the amount of adsorbed CO₂). **d** ln(P) vs 1/T plot for the results in **b**. **e** Heat of adsorption as a function of the amount of adsorbed CO₂ derived from the Clausius–Clapeyron equation and slopes in **b**. Error bars result from the uncertainty in our measurement of pressure.

To estimate the heat of adsorption (ΔH) of CO₂, the slopes of the plots of $\ln P$ vs $1/T$ (Fig. 1d) were analyzed using the Clausius–Clapeyron equation:

$$\Delta H = -R \frac{\partial(\ln P)}{\partial(T^{-1})}$$

The results are plotted in Fig. 1e as a function of the amount of adsorbed CO₂. The ΔH values ($17.9\text{--}22.4 \pm 2.5 \text{ kJ mol}^{-1}$) were in the range of physisorption instead of chemisorption^{56,57}.

Because CO₂ is adsorbed at hydrogen vacancies, the amount of CO₂ adsorbed was expected to increase with the number of hydrogen-deficient sites in the HB sheets (Fig. 1a). To determine the relationship between the amount of adsorbed CO₂ and the number of hydrogen vacancy sites, and to verify the reproducibility of CO₂ adsorption, we conducted five cycles of CO₂ adsorption/desorption using HB-473K, HB-523K, and HB-573K samples. According to the results of our gas chromatography analysis and the findings of previously reported thermal desorption spectroscopy analyses^{7,9}, the residual hydrogen occupancies (x in H_xB₁) for the HB-473K, HB-523K, and HB-573K samples were in the ranges of 0.81 < x < 0.95, 0.67 < x < 0.77, and 0.50 < x < 0.67, respectively. As described above, x is expressed as a range because its value is influenced by the differences in the hydrogen content between samples⁷ and the errors in temperature measurement. Figure 2a shows that the amount of adsorbed CO₂ remained unaltered when the experiments conducted using HB-473K and HB-523K were repeated. The amount of CO₂ adsorbed on HB-523K was greater than that on HB-473K, probably because the HB-523K sample had a greater number of hydrogen vacancy sites. However, the amount of CO₂ adsorbed on HB-573K was lower than that on HB-473K and HB-523K. Additionally, the amount of CO₂ adsorbed on HB-

573K decreased with continued cycling, indicating that the extensively hydrogen-deficient HB sheets (H_xB₁, 0.50 < x < 0.67) did not support reproducible CO₂ adsorption at 297 K.

To clarify the origin of the steady drop in CO₂ adsorption on HB-573K during cycling, the morphology and chemical state of the HB sheets were examined by scanning electron microscopy (SEM) and X-ray photoelectron spectroscopy (XPS) before and after heating at 573 K for 1 h. The SEM images before and after heating at 573 K (Fig. 2b, c, respectively) demonstrate slight agglomeration of the HB sheets by heating, suggestive of a reduction in the number of accessible adsorption sites consequently resulting in decreased CO₂ adsorption on HB-573K. However, the agglomeration cannot explain the steady decrease in CO₂ adsorption amount during the cycling experiments, because the same heating condition (573 K for 1 h) was used during each cycle, and the observed morphological change is likely to have been completed after the first cycle.

Two fundamental pathways for interaction between CO₂ and HB-573K during cycling (namely, desorption, and reaction) are suggested based on the XPS analysis (Supplementary Fig. 3). Specifically, heating at 573 K creates reactive sites in HB, some of which may be degraded by reacting with the adsorbed CO₂, while other reactive sites survive if the adsorbed CO₂ desorbs without reacting with them. Thus, these pathways can explain the accumulative degradation of HB-573K during cycling. Considering our previous results on the H₂ temperature programmed desorption (TPD) of HB sheets⁷, the temperature of 573 K corresponds to the terminus of the first desorption peak and the onset of the second desorption peak. The reactive sites are thus considered to correspond to the desorption component of the second desorption peak in TPD. Therefore, although reproducible adsorption/desorption was observed for HB-473K and HB-523K,

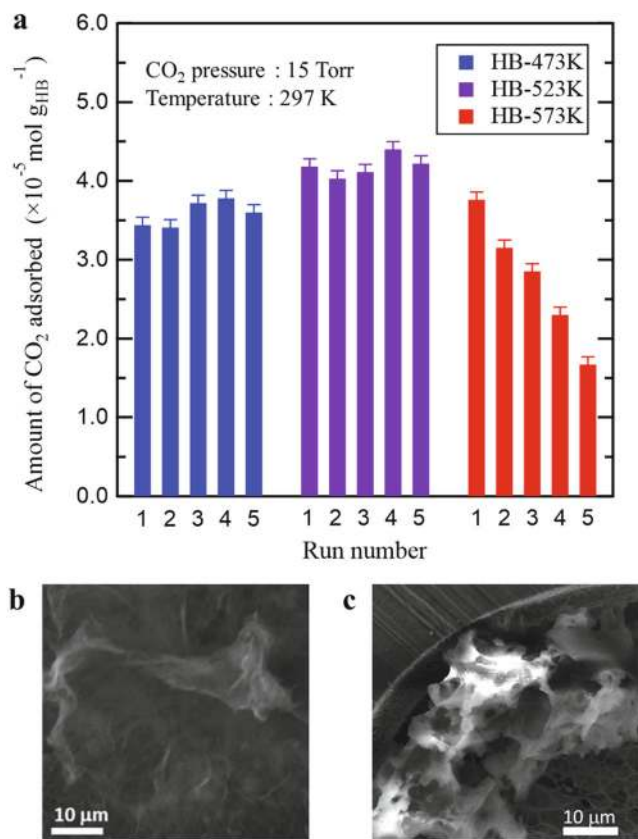


Fig. 2 Reproducibility of CO₂ adsorption on hydrogen boride (HB) sheets.

a Amount of adsorbed CO₂ plotted as a function of the number of adsorption/desorption cycles. Adsorption was performed at 297 K in CO₂ atmosphere (15 Torr); desorption was performed for 1 h at each temperature in vacuum (473 K, 523 K, and 573 K for HB-473K, HB-523K, and HB-573K, respectively). Error bars result from the uncertainty in our measurement of pressure. **b** Scanning electron microscopy (SEM) image of pristine HB sheets. **c** SEM image of HB sheets after heating to 573 K in ultrahigh vacuum for 1 h.

accumulative degradation of the CO₂ adsorptivity of HB-573 K occurred during cycling (Fig. 2a).

CO₂ molecules adsorb on HB-473K by Langmuir-type physisorption. Consequently, CO₂ may not adsorb on the hydrogen atoms at the outermost surface (bridge- and/or edge-type hydrogen atoms) of the HB sheets; however, it may adsorb on the hydrogen vacancy sites (i.e., on boron atoms) in HB-473K. Boron atoms that are not bound to hydrogen atoms can act as Lewis acid sites, with each boron atom adopting a simple *sp*² configuration comprising a vacant *p*_z orbital in its connection to the surrounding boron atoms. In this case, CO₂ may physisorb in an end-on configuration with one of the oxygen atoms of CO₂ close to the Lewis acid site of the boron atom. In contrast, if the charges in the HB sheets are sufficiently delocalized to supply electrons to the *p*_z orbital of a bare *sp*²-bonded boron atom (hydrogen vacancy), CO₂ may physisorb in a side-on configuration with the carbon atom of CO₂ close to the Lewis-base-like boron atom.

We conducted density functional theory (DFT) calculations to investigate the adsorption state of CO₂ on the HB sheets (Supplementary Figs. 4 and 5). Specifically, we calculated the potential energy surface (PES) on a grid over the primitive surface unit cell of the HB sheet by varying the distance between CO₂ and the HB sheet and the orientation of the CO₂ molecule with its molecular axis parallel to the surface (side-on configuration). The

HB sheet and CO₂ molecule were relaxed in their isolated states; therefore, no further relaxation was performed in the PES calculations. Thereafter, we calculated the interaction energy curves between CO₂ and HB to determine the most stable adsorption site (Fig. 3). For the pristine HB sheet, the CO₂ molecules were weakly adsorbed on the HB surface with an adsorption energy of 13–14 kJ mol⁻¹ and no distinct preferential adsorption site or orientation with respect to the surface (Fig. 3a, c and Supplementary Fig. 4). We also calculated the PES of CO₂ with its molecular axis perpendicular to the surface (end-on configuration) and discovered that it was less stable (Supplementary Fig. 6). These results indicated that CO₂ weakly physisorbs onto the pristine HB sheets, and CO₂ molecule(s) may behave like a 2D gas on the pristine HB sheet (i.e., free to rotate parallel to the surface and diffuse on HB sheets). However, when a hydrogen vacancy (*V*_H) was introduced, distinct differences in the adsorption energy (19–25 kJ mol⁻¹) were found depending on the adsorption site and molecular orientation with respect to the surface (Fig. 3b, d, and Supplementary Fig. 5). The CO₂ molecule preferentially adsorbed at the *V*_H sites in the side-on configuration, with a smaller adsorption height. The calculated adsorption energy was consistent with the experimentally obtained range of 17.9–22.4 ± 2.5 kJ mol⁻¹. The end-on configuration of CO₂ was also considered and discovered to be significantly less stable than the side-on configuration with *V*_H (Supplementary Fig. 6).

Despite the different crystallinity states observed for the HB sheets under experimental (amorphous) and theoretical (crystalline) conditions, the calculated and experimental adsorption energies were consistent, which indicates that the CO₂ molecules physisorb at the hydrogen vacancy sites in a side-on configuration, as shown in Fig. 3d. This implies that the boron atoms at the hydrogen-vacant sites act as weak Lewis bases in terms of charge. In particular, the charge of the HB sheets could be sufficiently delocalized to supply electrons to the *p*_z orbital of the bare *sp*²-bonded boron atom at the hydrogen vacancy site, which is consistent with the semimetal band structure of the HB sheets^{7,13}.

Thermal reaction products of HB sheets with CO₂. Hydrocarbon molecules such as methane (CH₄), ethane (C₂H₆), and propane (C₃H₈) are produced when HB sheets are heated in a CO₂ atmosphere at 523 K under moist conditions (Supplementary Fig. 7 and Supplementary Table 1). Therefore, CO₂ can be converted into hydrocarbons by reacting with the HB sheets. In this study, we focus primarily on CH₄ and C₂H₆ because C₃H₈ was only detected in small quantities.

Figure 4a shows the amount of C₂H₆ detected as a function of the cycle number without changing the HB sample (100 mg). The labels indicate the reactants supplied to the system in each cycle. C₂H₆ was verified by comparing its gas chromatography-mass spectrometry (GC-MS) signals with that of a standard gas of 100% C₂H₆ (Fig. 4b, c). Significant quantities of C₂H₆ were detected when the HB sheets were heated in CO₂ (10 cm³) in the presence of H₂O (0.1 cm³) at 523 K for 6 h (second and sixth cycles). Heating in CO₂ (first and third cycles), Ar (fourth cycle), and Ar containing H₂O (fifth cycle) produced smaller amounts of C₂H₆. Small quantities of C₂H₆ were detected in the fourth and fifth cycles although no carbon source was supplied. This observation was attributed to the residual carbon in the system from the first to the third cycles. The results described here clearly establish that the hydrogenation of CO₂ requires both HB sheets and H₂O. The results also indicate that the reaction is not continuous or catalytic, because the amount of C₂H₆ produced in the sixth cycle is lower than that produced in the second cycle.

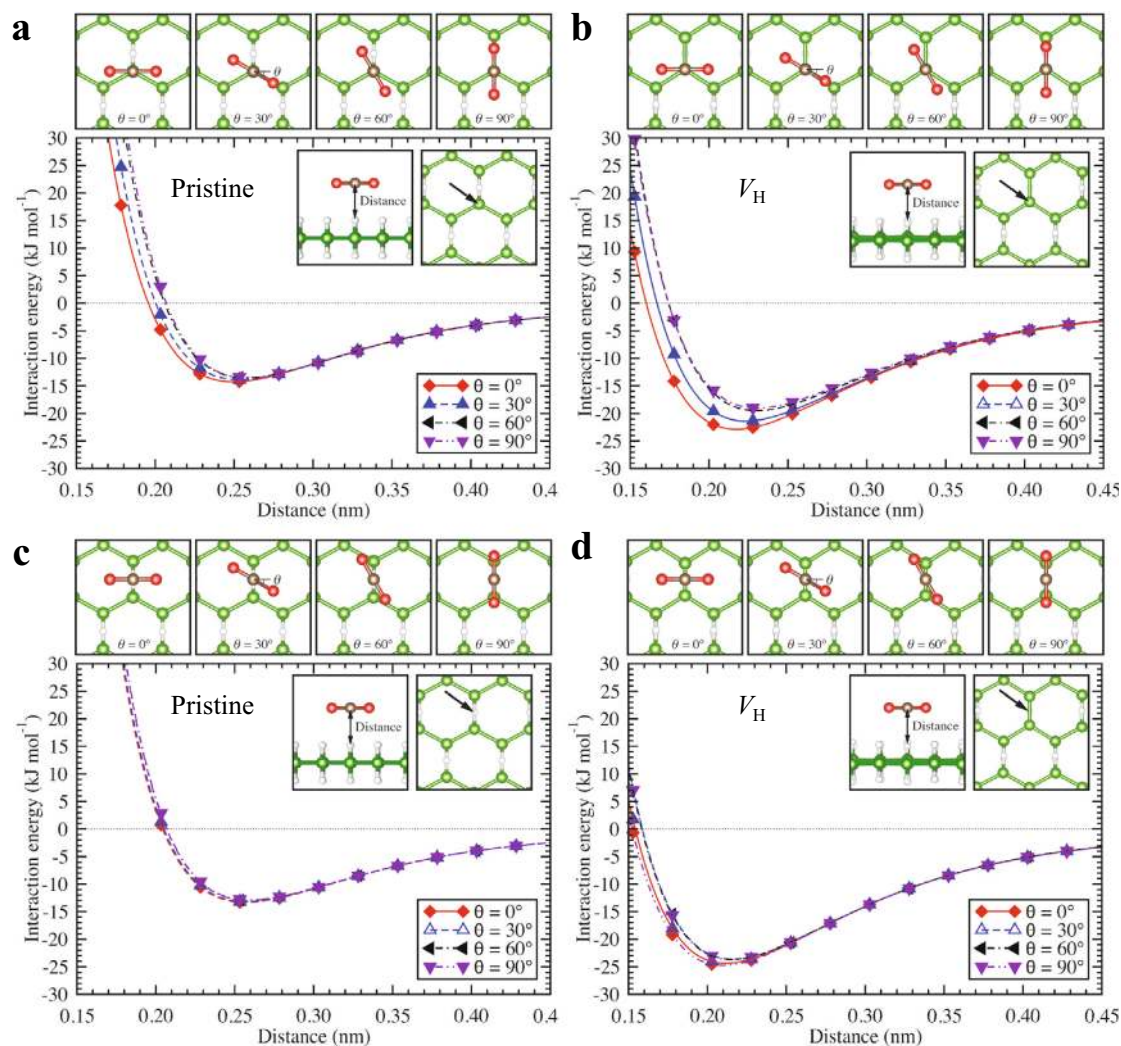
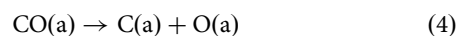
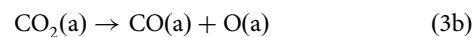
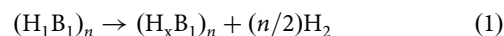


Fig. 3 Adsorption configurations and corresponding interaction energy (E_{int}) curves for CO_2 adsorption on hydrogen boride (HB) sheets with the side-on configuration. **a** E_{int} for the on-top B atom sites of the pristine HB sheet. **b** E_{int} for the on-top B atom sites of the H-vacant (V_{H}) HB sheet. **c** E_{int} for the on-top H sites of the pristine HB sheet. **d** E_{int} for the H-vacant sites of the H-vacant HB sheet. The distances are defined by the difference between the z-coordinate of CO_2 and the average z-coordinate of the surface H atoms of the HB sheets, as indicated in the inset figures. The adsorption sites are indicated by the arrows in the insets.

Figures 4d–f show the results of cycling experiments at different reaction temperatures (423, 473, 523, and 573 K) to elucidate the effect of temperature. Here, each cycle run was conducted sequentially using the same HB sample. As shown in Fig. 4d, H_2 was detected in every cycle, with the exception of the last cycle at 523 K, as a steady-state reaction product. The amount of H_2 detected decreased as the cycle temperature increased, indicating that the hydrogen in HB is consumed by the reaction. At 423 K, CH_4 and C_2H_6 were detected during cycling. The amounts of CH_4 and C_2H_6 detected were largest when CO_2 was introduced with H_2O (cycles 9 and 10), similar to the experiment shown in Fig. 4a. The amount of CH_4 detected increased with increasing reaction temperature, while that of C_2H_6 started to decrease at 573 K. These results indicate that the reaction between CO_2 and H in the HB sheets, including C–C coupling, starts to occur even at the relatively low temperature of 423 K. Furthermore, the amount of CH_4 produced exceeds that of C_2H_6 at 573 K, indicating that the rate of CH_4 desorption is faster than the rate of C–C coupling at 573 K. Finally, the fact that the final cycle at 523 K does not show reproducibility suggests that

degradation reaction may be occurring due to insufficient amount of hydrogen in the HB sheets.

The aforementioned results indicate that the presence of HB promotes C–C coupling and CO_2 conversion, considering that the products originate not only from simple hydrogenation using the hydrogen in HB, but also from bond rearrangements, such as C–C coupling. Furthermore, the detection of CO (Supplementary Fig. 7a and Supplementary Table 1) indicates that the dissociation of CO_2 can also occur on the HB sheets. The possible reaction steps are as follows:



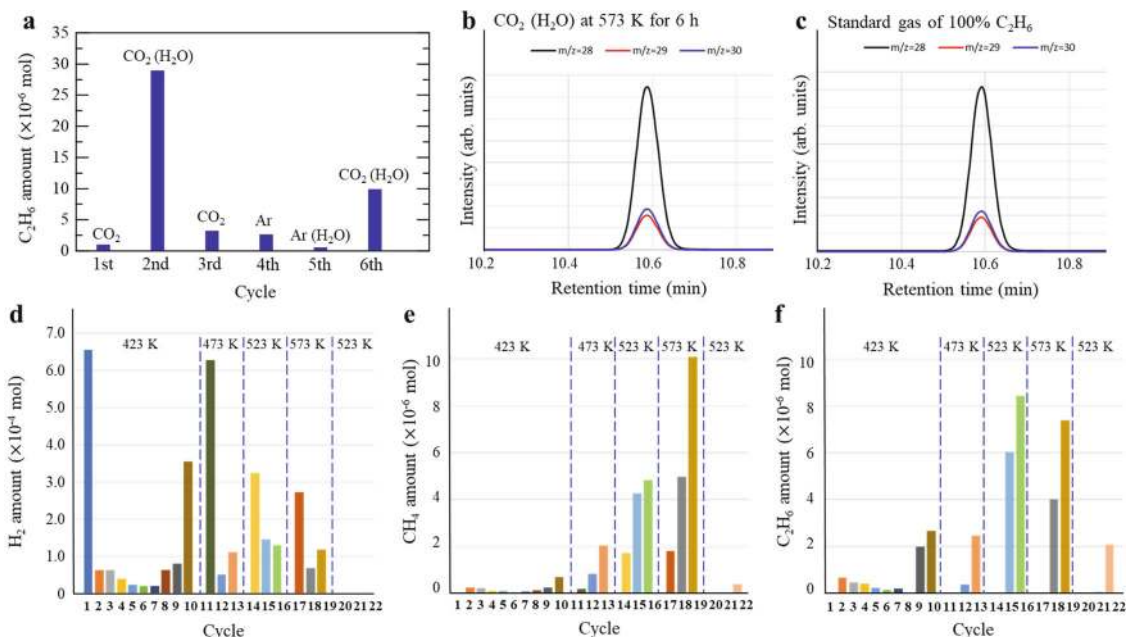
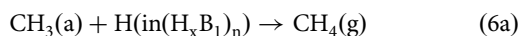
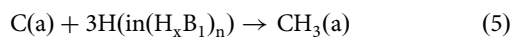


Fig. 4 Reaction product of CO_2 with hydrogen boride (HB) upon cycling. **a** Amount of C_2H_6 produced upon cycling. The labels identify the reactants supplied to the system in each cycle. Before the measurements, the HB sample was heated at 523 K for 6 h in Ar to create hydrogen vacancies in the HB sheets (100 mg). For each cycle, the gas was changed to CO_2 or Ar at 300 K, and the HB sheets were heated at 373 K in a flow of CO_2 or Ar. In the second, fifth, and sixth cycles, when the temperature reached 373 K, 0.1 cm^3 of H_2O was added to the system using a syringe. Thereafter, the reactor was closed, the gas flow was stopped, and the temperature was increased to 523 K. The sample was held at 523 K for 6 h. **b, c** Mass patterns of detected gas and standard gas. The reaction products were analyzed using gas chromatography-mass spectrometry (GC-MS). C_2H_6 was verified by comparing its GC-MS signal (**b**) with that of standard gas of 100% C_2H_6 (**c**). **d–f** Amounts of (**d**) H_2 , (**e**) CH_4 , and (**f**) C_2H_6 produced upon cycling by continuously using the same HB sample (100 mg). The atmospheres used for each cycle (6 h) were as follows. At 423 K: cycles 1–7, Ar gas; cycle 8, CO_2 gas; cycles 9 and 10, $\text{CO}_2 + 0.1 \text{ cm}^3 \text{ H}_2\text{O}$. At 473, 523, 573, and again 523 K: cycles 11, 14, 17, and 20, Ar flow; cycles 12, 15, 18, and 21: Ar gas; cycles 13, 16, 19, and 22, $\text{CO}_2 + 0.1 \text{ cm}^3 \text{ H}_2\text{O}$. The experiments were performed from left to right along the horizontal axis.



where $(\text{H}_1\text{B}_1)_n$ and $(\text{H}_x\text{B}_1)_n$ denote pristine and hydrogen deficient HB sheets, respectively, (g) and (a) represent the gas and adsorbed states, respectively, and $0.67 < x < 0.77$. Reactions (1) and (2) are supported by the results in Fig. 1. Reaction (3a) is supported by the detection of CO (Supplementary Figs. 7a, and 8a and Supplementary Table 1). Reactions (6a) and (6b) are supported by the results in Figs. 4d–f.

To investigate the presence of residual reaction products on the HB sheets, such as O(a) in reaction (3), we conducted thermogravimetric analysis (TGA) of the HB sheets under Ar or CO_2 flow and performed post-experimental analysis of the samples by XPS and X-ray diffraction (XRD) analyses, the results of which are shown in Fig. 5 and Supplementary Figs. 9 and 10. When the HB sheets were heated in Ar, the weight of the sample began decreasing at 400 K (Fig. 5a). By comparing with our previously reported thermal desorption spectroscopy results^{7,9}, this change was attributed to hydrogen release. When heated under CO_2 flow, the weight of the sample still began decreasing at 400 K, as in the case of Ar flow; however, it subsequently began to increase at 466 K (Fig. 5b). The net increase in weight reached a maximum of 5.4% at 734 K. This increase indicates that HB reacted with CO_2 and that the reaction products remaining on the sample compensated for the weight of lost hydrogen. The post-experimental XPS analysis of the samples indicated that oxygen

was the principal element remaining on the HB sheets (Fig. 5c). The intensity of the O 1s peak clearly increased with increasing treatment temperature, whereas the intensity of the C 1s peak remained unchanged. The XPS results were consistent with the process proposed in reactions (4)–(6), wherein oxygen remained on the surface while carbon was desorbed as CH_4 or C_2H_6 . The C 1s and O 1s XPS peaks were detected even for fresh HB sheets at 300 K, and were attributed to the adventitious carbon and traces of oxygen on the Au substrate. Overall, the XPS survey scan and XRD results verified that the sample was free of impurities (Supplementary Figs. 9 and 10).

There are two possible roles for H_2O in the conversion of CO_2 : (i) as a promoter of reactions (3)–(6) by forming a specific, perhaps catalytic, intermediate; and (ii) as a hydrogen source for the hydrogen vacancies in the HB sheets. Recent experiments have shown that proton exchange occurs on HB sheets in liquid water⁵⁸. Therefore, water may accept a proton from HB to form H_3O^+ , which can participate in redox reactions accompanied by electron transfer within HB, or in proton transfer reactions without the application of an external field, as in the rusting of iron. The identification of water as the hydrogen source in the hydrogenation reaction is supported by the effect of H_2O on the conversion of ethanol on hydrogen-deficient HB sheets⁹. In the previous study, the presence of water influenced the product distribution by extensively promoting hydrogenation, which increased the selectivity toward C_2H_6 relative to C_2H_4 ⁹. We plan to examine the role of water and the proposed reaction pathways (1)–(6) using in situ spectroscopy with collective knowledge from theoretical calculations in our future work.

The detection of C_2H_6 as a CO_2 reaction product demonstrates that the hydrogen-deficient HB sheets significantly promoted

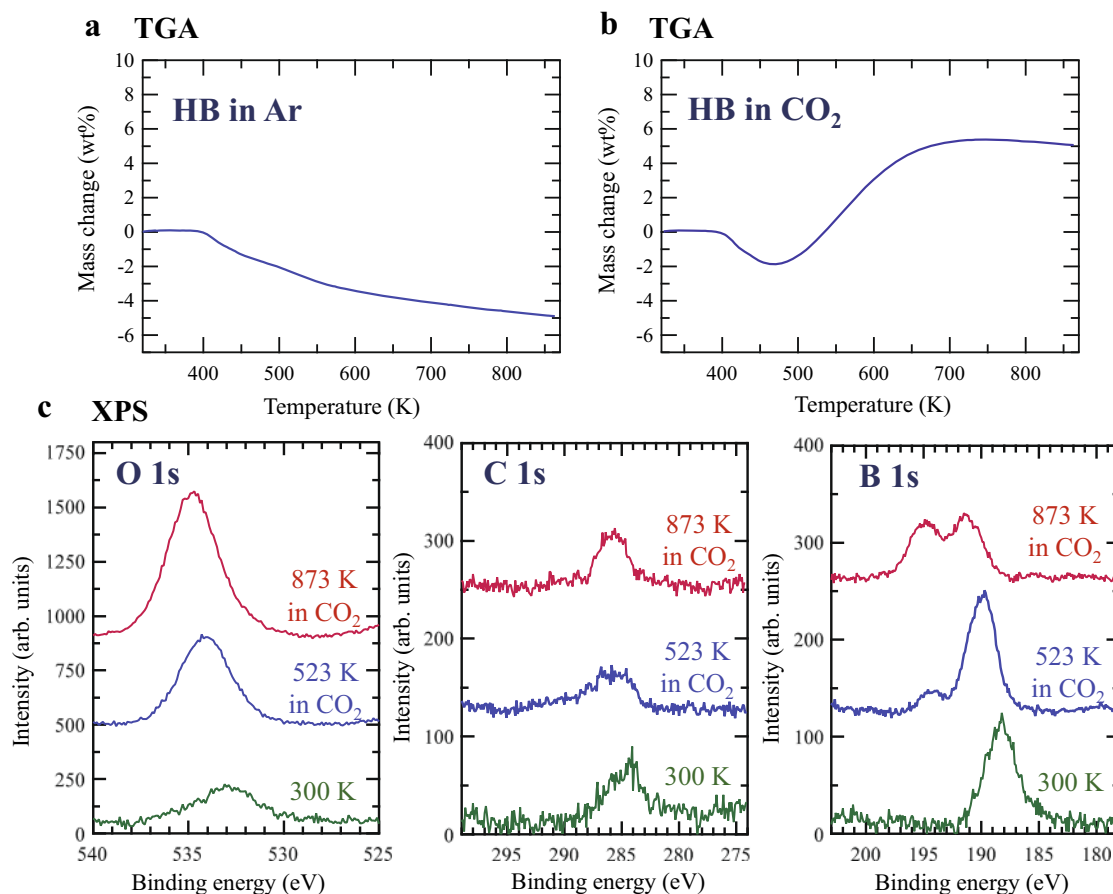


Fig. 5 Changes in hydrogen boride (HB) sheets upon heating under various reaction conditions. Thermogravimetric analysis (TGA) of the HB sheets in flows of **a** Ar and **b** CO₂. **c** O 1s, C 1s, and B 1s XPS spectra of HB sheets at 300 K following heating at 523 K in CO₂, and at 873 K in CO₂.

C–C coupling and CO₂-conversion reactions. Both CO₂ conversion^{33,34} and C–C coupling^{59,60} have been observed in boron-based homogeneous organic molecular catalysts, wherein the strong Lewis acidity and low electronegativity of boron permit it to mediate C–C coupling. However, our results clearly demonstrate that a solid material comprised solely of boron and hydrogen can accomplish both C–C coupling and CO₂ conversion. It is likely that some of the hydrogen-deficient sites (boron sites) of HB sheets possess similar electronic states to the active sites in boron-based homogeneous organic molecular catalysts. In any case, the findings here indicate that HB sheets may be employed as a heterogeneous catalyst or catalyst support for CO₂ conversion. This finding requires further analysis and system optimization, including the addition of an appropriate hydrogen source.

Conclusion

In this work, we examined the adsorption and conversion efficiency of CO₂ using HB sheets. Whereas fresh HB failed to adsorb CO₂ at 297 K, hydrogen-deficient HB sheets preheated at 473 K (H_xB₁, 0.81 < x < 0.98) reproducibly physisorbed CO₂. The adsorption mechanism followed the Langmuir model with saturation coverage of 2.4 × 10⁻⁴ mol g⁻¹ at 297 K and heat of adsorption of ~20 kJ mol⁻¹. This behavior suggests that only some of the hydrogen vacancy sites in the hydrogen-deficient HB sheets provide suitable sites for CO₂ adsorption. In contrast, the extensively hydrogen-deficient HB sheet (H_xB₁, 0.50 < x < 0.67) did not show reproducible CO₂ adsorption performance at 297 K, presumably due to the chemical changes caused by the release of an excessive amount of hydrogen upon heating. When a fresh HB

sheet was heated in a flow of CO₂, HB began reacting with CO₂ at 423 K in its hydrogen-deficient state. Notably, at 423 K and under a moist atmosphere, CH₄ and C₂H₆ were detected as the products of the reaction between CO₂ and the HB sheets, indicating that hydrogen-deficient HB promotes both C–C coupling and CO₂ conversion reactions. Although CO₂ conversion^{33,34} and C–C coupling^{59,60} have been previously exhibited by boron-based molecular systems, our results show that a solid material comprised solely of boron and hydrogen can accomplish both C–C coupling and CO₂ conversion. Our results also indicate that HB sheets bear significant potential as heterogeneous catalysts or catalyst supports for CO₂ conversion. However, further detailed analysis is required for the design of optimized systems, including the selection of an appropriate hydrogen source or supply, with the objective of achieving continuous catalytic CO₂ conversion.

Methods

Synthesis of HB sheets. The HB sheets were prepared using previously reported ion-exchange methods^{7–11,14}. Specifically, MgB₂ powder (1.0 g, 99%, Rare Metallic Co., Ltd., Tokyo, Japan) in acetonitrile (300 mL, 99.5%, Wako Pure Chemical Industries Ltd., Osaka, Japan) was added to a mixture of an ion-exchange resin (60 mL, Amberlite IR120B hydrogen, Organo Corp., Tokyo, Japan) and acetonitrile (200 mL) in a Schlenk flask in a nitrogen atmosphere. Water was carefully removed due to the facile hydrolysis of MgB₂⁶¹. The resulting mixture was stirred with a magnetic stirrer at 400 rpm for 3 d at room temperature (~300 K). We did not apply the recently reported acid-assisted reaction⁶². The reaction mixture was allowed to settle for a sufficient time (a few hours), whereafter the supernatant was collected and stored for 1 d at 255 K to physically separate the B(OH)₃ by-product. For samples containing unreacted materials such as the oxides present in the starting materials, the reaction mixture was filtered through a 0.2-μm pore filter (Omnipore Membrane Filters, Merck Millipore, Billerica, MA, USA), and the filtrate was stored for 1 d at 255 K to physically separate the B(OH)₃ by-product. The dried HB sheets were prepared by heating the resulting liquid at 343 K, and the gas

that evaporated during heating was pumped through a liquid nitrogen trap. We characterized the product rigorously using XPS (JPS 9010 TR, JEOL, Ltd., Tokyo, Japan) to confirm the absence of Mg, the presence of negatively charged B, and the absence of oxidized B^{7-11,14}.

CO₂ adsorption measurements. CO₂ adsorption measurements were conducted using a custom-made experimental system. The HB sample (30–50 mg) was placed at the bottom of a quartz tube in a He atmosphere and evacuated to a high vacuum (~10⁻⁶ Torr) using a Hickman-type oil diffusion pump (Makuhari Rikagaku Glass Inc., Chiba, Japan) and an oil rotary pump (GVD-165A, ULVAC, Japan) via a liquid nitrogen trap. The pressure was monitored using a capacitance manometer (Baratron Type622, MKS Instruments Japan Co., Tokyo, Japan) and a Pirani vacuum gauge (Wakaida Science Co., Tokyo, Japan). Both pressure gauges were connected to a WVG-IT unit (Wakaida Science Co., Tokyo, Japan) to display the pressure. The sample temperature was monitored using a type-K thermocouple attached to the exterior of the quartz glass close to the sample. The sample temperature was controlled using an electric heater equipped with a temperature controller (RTC5630, Okura Ltd., Japan). We used ice water to achieve a temperature of 273 K, and a mixture of ethanol, ice (400 mL), and NaCl (15 g) to achieve a temperature of 253 K.

Analysis of thermal reaction products. The thermal reaction products between the HB sheets and CO₂ were examined using a home-built experimental system. Fresh HB sheets (100 mg) were placed in a quartz tube (10 cm³) with quartz wool and heated to 523 K in a flow of CO₂. After reaching 523 K, we closed the valves on the CO₂ flow line to achieve a batch reaction system. This method was employed for the experiments shown in Supplementary Fig. 6 and Supplementary Table 1; whereas, for the experiments shown in Fig. 4 and Supplementary Fig. 7, the valves were closed at 373 K to avoid the flow of the products during heating to 573 K. After closing the valves, we introduced 0.1 cm³ of distilled water into the system using a syringe because the introduction of water enhanced the conversion of CO₂ (see main text “Thermal reaction products of HB sheets with CO₂”). After 6 h, we extracted the interior gas (1.0 cm³) using a syringe. The extracted gas was analyzed using a gas chromatographer (GC-8A, Shimadzu Corporation, Ltd., Kyoto, Japan) equipped with 5A molecular sieves (60–80 mesh, GL Sciences, Inc.) and a Porapak Q column (50–80 mesh, Waters Chromatography Ireland Ltd.). We also examined the gas samples via GC-MS (Shimadzu GC-MS-QP2010 Plus, Shimadzu Corporation, Ltd., Kyoto, Japan) using a GC equipped with a Shimadzu SH-Rt-Msieve 5A column. Helium was used as the carrier gas, and supplied at 50.4 cm s⁻¹. When we continued to use the same HB sample, the gas inside the tube was replaced using He (for the experiments shown in Supplementary Fig. 6 and Supplementary Table 1), Ar, or CO₂ (the gas used for the subsequent experimental cycle shown in Fig. 4 and Supplementary Fig. 7) at room temperature (~300 K), and finally replaced with CO₂.

X-ray photoelectron spectroscopy. XPS measurements were conducted at room temperature (~298 K) using a JPS 9010 TR spectrometer (JEOL, Ltd., Japan) equipped with an ultrahigh vacuum chamber and an Al K α X-ray source (1486.6 eV). The pass energy was 10 eV, the energy resolution (estimated from the Ag 3d_{5/2} peak width of a clean Ag sample) was 0.635 eV, and the binding energy uncertainty was ± 0.05 eV. The sample was placed on an Au surface (Au sheet, Au-173421, 99.95%, Nilaco Co. Ltd.). The Shirley background was subtracted from the spectrum using SpecSurf version 1.8.3.7 (JEOL, Ltd., Japan). The charge build-up in the sample (due to the incomplete contact of the Au sheet with the sample holder of the apparatus) caused a slight shift to higher binding energies for those spectra. Therefore, we calibrated the charge build-up based on the Au 4f_{7/2} peak as 84.0 eV.

Thermogravimetric analysis. TGA was performed using an STA 2500 Regulus apparatus (Netzsch Japan, Ltd., Japan). Initially, ~10 mg of HB sheets were placed in an Al₂O₃ crucible in the apparatus under vacuum, which was followed by the introduction of Ar at 20 mL min⁻¹. Thereafter, the sample was heated at 373 K for 30 min in a 10 mL min⁻¹ flow of Ar to remove the adsorbed water, and subsequently cooled to 323 K. Finally, the TGA measurements were performed up to 873 K at a heating rate of 10 K min⁻¹ in a 100 mL min⁻¹ flow of Ar or CO₂.

X-ray diffraction. The XRD patterns were recorded at room temperature (~300 K) using a benchtop X-ray diffractometer (Rigaku MiniFlex, Tokyo, Japan) employing Cu K α radiation. The X-rays were generated using the line focus principle. A reflection-free Si plate was used as the sample stage. The diffraction patterns were recorded using a D/teX Ultra silicon strip detector (Rigaku) at 0.01° s⁻¹ up to a 2θ value of 90°.

Scanning electron microscopy. SEM measurements were performed on a JSM-521 (JEOL, Ltd., Japan) operating at 10 kV. Samples were placed on Cu-TEM grids.

Density functional theory. Periodic DFT calculations were performed using the Quantum-ESPRESSO package^{63–66}. The electron–ion interactions were described using the GBRV⁶⁷ ultrasoft pseudopotentials⁶⁸ and the wave functions were expanded in terms of the plane-wave basis set. The rev-vdW-DF2^{69,70} functional

was used for the exchange correlation. A CO₂ molecule was placed in a 4 × 4 supercell, and the effective screening medium method^{71,72} was used to eliminate spurious electrostatic interactions between neighboring HB sheets. Further details can be found in ref. 58. The interaction (potential) energy (E_{int}) was defined as $E_{\text{int}} = E_{\text{tot}}(\text{CO}_2/\text{HB}) - E_{\text{tot}}(\text{CO}_2) - E_{\text{tot}}(\text{HB})$, where $E_{\text{tot}}(\text{CO}_2/\text{HB})$, $E_{\text{tot}}(\text{CO}_2)$, and $E_{\text{tot}}(\text{HB})$ are the total energies of the adsorption system, CO₂ molecules in the gas phase, and free-standing HB sheets, respectively. The adsorption energy was defined as the negative of the interaction energy ($-E_{\text{int}}$) at the equilibrium height.

Data availability

All results are reported in the main paper and Supplementary Information. Input and output files for Quantum-ESPRESSO^{63–66} calculations are available on the Materials Cloud Archive⁷³. All other data are available from the authors upon reasonable request.

Received: 4 March 2022; Accepted: 22 September 2022;

Published online: 04 October 2022

References

- Fiori, G. et al. Electronics based on two-dimensional materials. *Nat. Nanotechnol.* **9**, 768–779 (2014).
- Chia, X. & Pumera, M. Characteristics and performance of two-dimensional materials for electrocatalysis. *Nat. Catal.* **1**, 909–921 (2018).
- Deng, D. et al. Catalysis with two-dimensional materials and their heterostructures. *Nat. Nanotechnol.* **11**, 218–230 (2016).
- Jin, H. et al. Emerging two-dimensional nanomaterials for electrocatalysis. *Chem. Rev.* **118**, 6337–6408 (2018).
- Luo, B., Liu, G. & Wang, L. Recent advances in 2D materials for photocatalysis. *Nanoscale* **8**, 6904–6920 (2016).
- Tan, C. et al. Recent advances in ultrathin two-dimensional nanomaterials. *Chem. Rev.* **117**, 6225–6331 (2017).
- Nishino, H. et al. Formation and characterization of hydrogen boride sheets derived from MgB₂ by cation exchange. *J. Am. Chem. Soc.* **139**, 13761–13769 (2017).
- Tominaka, S. et al. Geometrical frustration of B–H bonds in layered hydrogen borides accessible by soft chemistry. *Chem.* **6**, 406–418 (2020).
- Fujino, A. et al. Hydrogenated borophene shows catalytic activity as solid acid. *ACS Omega* **4**, 14100–14104 (2019).
- Fujino, A. et al. Ethanol–ethylene conversion mechanism on hydrogen boride sheets probed by in situ infrared absorption spectroscopy. *Phys. Chem. Chem. Phys.* **23**, 7724–7734 (2021).
- Ito, S. I. et al. Hydrogen boride sheets as reductants and the formation of nanocomposites with metal nanoparticles. *Chem. Lett.* **49**, 789–793 (2020).
- Gao, S. et al. 2D hydrogenated boride as a reductant and stabilizer for in situ synthesis of ultrafine and surfactant-free carbon supported noble metal electrocatalysts with enhanced activity and stability. *J. Mater. Chem. A* **8**, 18856–18862 (2020).
- Tateishi, I. et al. Semimetallicity of free-standing hydrogenated monolayer boron from MgB₂. *Phys. Rev. Mater.* **3**, 024004 (2019).
- Kawamura, R. et al. Photoinduced hydrogen release from hydrogen boride sheets. *Nat. Commun.* **10**, 4880 (2019).
- Jiao, Y., Ma, F., Bell, J., Bilic, A. & Du, A. Two-dimensional boron hydride sheets: high stability, massless Dirac fermions, and excellent mechanical properties. *Angew. Chem. Int. Ed.* **55**, 10292–10295 (2016).
- Mortazavi, B. et al. Borophene hydride: a stiff 2D material with high thermal conductivity and attractive optical and electronic properties. *Nanoscale* **10**, 3759–3768 (2018).
- He, J. et al. Orbital driven giant thermal conductance associated with abnormal strain dependence in hydrogenated graphene-like borophene. *npj Comput. Mater.* **5**, 47 (2019).
- Shukla, V., Araujo, R. B., Jena, N. K. & Ahuja, R. Borophene’s tryst with stability: exploring 2D hydrogen boride as an electrode for rechargeable batteries. *Phys. Chem. Chem. Phys.* **20**, 22008–22016 (2018).
- Makaremi, M., Mortazavi, B. & Singh, C. V. 2D hydrogenated graphene-like borophene as a high capacity anode material for improved Li/Na ion batteries: a first principles study. *Mater. Today Energy* **8**, 22–28 (2018).
- Abtey, T. A., Shih, B. C., Dev, P., Crespi, V. H. & Zhang, P. Prediction of a multicenter-bonded solid boron hydride for hydrogen storage. *Phys. Rev. B* **83**, 094108 (2011).
- Abtey, T. A. & Zhang, P. Charging-assisted hydrogen release mechanism in layered boron hydride. *Phys. Rev. B* **84**, 094303 (2011).
- Chen, L. et al. Reversible hydrogen storage in pristine and Li decorated 2D boron hydride. *Phys. Chem. Chem. Phys.* **20**, 30304–30311 (2018).

23. An, Y. et al. Unveiling the electric-current-limiting and photodetection effect in two-dimensional hydrogenated Borophene. *Phys. Rev. Appl.* **11**, 064031 (2019).
24. Kumawat, R. L., Jena, M. K. & Pathak, B. Individual identification of amino acids on an atomically thin hydrogen boride system using electronic transport calculations. *J. Phys. Chem. C* **124**, 27194–27202 (2020).
25. Xiang, P., Chen, X., Xiao, B. & Wang, Z. M. Highly flexible hydrogen boride monolayers as potassium-ion battery anodes for wearable electronics. *ACS Appl. Mater. Interfaces* **11**, 8115–8125 (2019).
26. Cuong, N. T. et al. Topological Dirac nodal loops in nonsymmorphic hydrogenated monolayer boron. *Phys. Rev. B* **101**, 195412 (2020).
27. Oliva-Enrich, J. M., Kondo, T., Alkorta, I., Elguero, J. & Klein, D. J. Diborane concatenation leads to new planar boron chemistry. *ChemPhysChem* **21**, 2460–2467 (2020).
28. Ploysongsri, N., Vchirawongkwin, V. & Ruangpornvisuti, V. Hydrogen boride nanotubes and their C, N, O decoration and doping derivatives as materials for hydrogen-containing gases storage and sensing: a SCC–DFTB study. *Vacuum* **187**, 110140 (2021).
29. Lei, B., Zhang, Y. Y. & Du, S. X. Band engineering of B₂H₂ nanoribbons. *Chin. Phys. B* **28**, 046803 (2019).
30. Ozin, G. & Siler, T. Catalyst: new materials discovery: machine-enhanced human creativity. *Chem.* **4**, 1183–1189 (2018).
31. Chen, X.-M. & Chen, X. Chemical syntheses of two-dimensional boron. *Chem* **6**, 324–326 (2020).
32. Klein, D. J., Ferrer, M., Elguero, J., Bytautas, L. & Oliva-Enrich, J. M. Hückeloid model for planar boranes. *Theor. Chem. Acc.* **140**, 55 (2021).
33. Bontemps, S. Boron-mediated activation of carbon dioxide. *Coord. Chem. Rev.* **308**, 117–130 (2016).
34. Stoy, A. et al. CO₂ binding and splitting by boron–boron multiple bonds. *Angew. Chem. Int. Ed.* **57**, 5947–5951 (2018).
35. Liu, G. et al. Elemental boron for efficient carbon dioxide reduction under light irradiation. *Angew. Chem. Int. Ed.* **56**, 5570–5574 (2017).
36. Sun, Q., Wang, M., Li, Z., Du, A. & Searles, D. J. A computational study of carbon dioxide adsorption on solid boron. *Phys. Chem. Chem. Phys.* **16**, 12695–12702 (2014).
37. Santos-Putungan, A. B., Stojić, N., Binggeli, N. & Paraan, F. N. C. Strong chemisorption of CO₂ on B₁₀–B₁₃ planar-type clusters. *J. Phys. Condens. Matter* **31**, 145504 (2019).
38. Santos-Putungan, A. B., Stojić, N., Binggeli, N. & Paraan, F. N. C. Selective capture of CO₂ over N₂ and CH₄: B clusters and their size effects. *Mater. Today Commun.* **22**, 100712 (2020).
39. Luo, W. et al. First-principles study of χ_3 -borophene for charge-modulated switchable CO₂ capture. *Phys. Chem. Chem. Phys.* **22**, 8864–8869 (2020).
40. Tan, X., Tahini, H. A. & Smith, S. C. Borophene as a promising material for charge-modulated switchable CO₂ capture. *ACS Appl. Mater. Interfaces* **9**, 19825–19830 (2017).
41. Qin, G., Cui, Q., Du, A. & Sun, Q. Borophene: a metal-free and metallic electrocatalyst for efficient converting CO₂ into CH₄. *ChemCatChem* **12**, 1483–1490 (2020).
42. Gao, G. et al. Modelling CO₂ adsorption and separation on experimentally-realized B₄₀ fullerene. *Comp. Mater. Sci.* **108**, 38–41 (2015).
43. Dong, H. et al. B₄₀ fullerene: an efficient material for CO₂ capture, storage and separation. *Curr. Appl. Phys.* **15**, 1084–1089 (2015).
44. Qu, M., Qin, G., Du, A., Fan, J. & Sun, Q. B₈₀ fullerene: a promising metal-free photocatalyst for efficient conversion of CO₂ to HCOOH. *J. Phys. Chem. C* **123**, 24193–24199 (2019).
45. Sun, Q., Wang, M., Li, Z., Du, A. & Searles, D. J. Carbon dioxide capture and gas separation on B₈₀ fullerene. *J. Phys. Chem. C* **118**, 2170–2177 (2014).
46. Taylor, J. W., McSkimming, A., Essex, L. A. & Harman, W. H. CO₂ reduction with protons and electrons at a boron-based reaction centre. *Chem. Sci.* **10**, 9084–9090 (2019).
47. Zhao, Y., Zhang, Z., Qian, X. & Han, Y. Properties of carbon dioxide absorption and reduction by sodium borohydride under atmospheric pressure. *Fuel* **142**, 1–8 (2015).
48. Lombardo, L., Yang, H., Zhao, K., Dyson, P. J. & Züttel, A. Solvent- and catalyst-free carbon dioxide capture and reduction to formate with borohydride ionic liquid. *ChemSusChem* **13**, 2025–2031 (2020).
49. Lombardo, L., Ko, Y., Zhao, K., Yang, H. & Züttel, A. Direct CO₂ capture and reduction to high-end chemicals with tetraalkylammonium borohydrides. *Angew. Chem. Int. Ed.* **60**, 9580–9589 (2021).
50. Kadota, K., Sivaniyah, E. & Horike, S. Reactivity of borohydride incorporated in coordination polymers toward carbon dioxide. *Chem. Commun.* **56**, 5111–5114 (2020).
51. Sun, Q. et al. Charge-controlled switchable CO₂ capture on boron nitride nanomaterials. *J. Am. Chem. Soc.* **135**, 8246–8253 (2013).
52. Tang, S. et al. Metal-free boron nitride nanoribbon catalysts for electrochemical CO₂ reduction: combining high activity and selectivity. *ACS Appl. Mater. Interfaces* **11**, 906–915 (2019).
53. Qu, M., Qin, G., Fan, J., Du, A. & Sun, Q. Boron-rich boron nitride nanomaterials as efficient metal-free catalysts for converting CO₂ into valuable fuel. *Appl. Surf. Sci.* **555**, 149652 (2021).
54. Tang, M., Shen, H., Xie, H. & Sun, Q. Metal-free catalyst B₂S sheet for effective CO₂ electrochemical reduction to CH₃OH. *ChemPhysChem* **21**, 779–784 (2020).
55. Mou, S. et al. Boron phosphide nanoparticles: a nonmetal catalyst for high-selectivity electrochemical reduction of CO₂ to CH₃OH. *Adv. Mater.* **31**, e1903499 (2019).
56. Lennard-Jones, J. E. Processes of adsorption and diffusion on solid surfaces. *Trans. Faraday Soc.* **28**, 333–359 (1932).
57. Norsko, J. K. Chemisorption on metal surfaces. *Rep. Prog. Phys.* **53**, 1253–1295 (1990).
58. Rojas, K. I. M. et al. Chemical stability of hydrogen boride nanosheets in water. *Commun. Mater.* **2**, 81 (2021).
59. Shoji, Y. et al. Boron-mediated sequential alkyne insertion and C–C coupling reactions affording extended π -conjugated molecules. *Nat. Commun.* **7**, 12704 (2016).
60. Rao, B. & Kinjo, R. Boron-based catalysts for C–C bond-formation reactions. *Chem. Asian J.* **13**, 1279–1292 (2018).
61. Nishino, H. et al. Formation mechanism of boron-based nanosheet through the reaction of MgB₂ with water. *J. Phys. Chem. C* **121**, 10587–10593 (2017).
62. Kawamura, R. et al. Acid assisted synthesis of HB sheets through exfoliation of MgB₂ bulk in organic media. *Chem. Lett.* **49**, 1194–1196 (2020).
63. Giannozzi, P. et al. QUANTUM ESPRESSO: a modular and open-source software project for quantum simulations of materials. *J. Phys. Condens. Matter* **21**, 395502 (2009).
64. Giannozzi, P. et al. Advanced capabilities for materials modelling with Quantum ESPRESSO. *J. Phys. Condens. Matter* **29**, 465901 (2017).
65. Sabatini, R., Küçükbenli, E., Kolb, B. & Thonhauser, T. & De Gironcoli, S. Structural evolution of amino acid crystals under stress from a non-empirical density functional. *J. Phys. Condens. Matter* **24**, 424209 (2012).
66. Thonhauser, T. et al. Van der Waals density functional: Self-consistent potential and the nature of the van der Waals bond. *Phys. Rev. B* **76**, 125112 (2007).
67. Garrity, K. F., Bennett, J. W., Rabe, K. M. & Vanderbilt, D. Pseudopotentials for high-throughput DFT calculations. *Comp. Mater. Sci.* **81**, 446–452 (2014).
68. Vanderbilt, D. Soft self-consistent pseudopotentials in a generalized eigenvalue formalism. *Phys. Rev. B Condens. Matter* **41**, 7892–7895 (1990).
69. Hamada, I. Van der Waals density functional made accurate. *Phys. Rev. B* **89**, 121103 (2014).
70. Callsen, M. & Hamada, I. Assessing the accuracy of the van der Waals density functionals for rare-gas and small molecular systems. *Phys. Rev. B* **91**, 195103 (2015).
71. Otani, M. & Sugino, O. First-principles calculations of charged surfaces and interfaces: a plane-wave nonrepeated slab approach. *Phys. Rev. B* **73**, 115407 (2006).
72. Hamada, I., Otani, M., Sugino, O. & Morikawa, Y. Green’s function method for elimination of the spurious multipole interaction in the surface/interface slab model. *Phys. Rev. B* **80**, 165411 (2009).
73. Goto, I. et al. Carbon dioxide adsorption and conversion to methane and ethane on hydrogen boride sheets. *Materials Cloud Archive* 2022.112 (2022).

Acknowledgements

This work was supported by the MEXT Element Strategy Initiative to Form Core Research Center (JPMXP0112101001), JSPS KAKENHI (Grant Nos. JP18K18989, JP19H02551, JP21H05012, and Hydrogenomics [JP19H05046:A01, JP21H00015:B01, and JP18H05519:A05-2]), JST CREST (Grant No. JPMJCR21O4), and MHI Innovation Accelerator LLC. We thank professor Shinichiro Noro for his help with the preliminary experiments. We thank professor Kenichi Shimizu for his useful insights on the reactivity of HB. We thank professor Junji Nakamura for his insightful discussions on the adsorption of CO₂. Numerical calculations were performed using the Numerical Materials Simulator at the National Institute for Materials Science.

Author contributions

T.K. conceived the project and supervised the experimental part of the project with the support of H.H. I.H. conducted the DFT calculations. T.G. and S.I. prepared the sample and carried out the CO₂ adsorption experiments. T.G., S.I., and S.L.S. conducted the CO₂ conversion experiments. T.G. carried out the TGA and the XRD experiments. R.I. conducted the SEM analysis. T.G., R.I., T.K., and I.M. conducted the XPS analysis. T.G., S.I., S.L.S., R.I., Y.H., I.H., and T.K. analyzed the results. All authors discussed the results and helped edit the manuscript. T.K. wrote the manuscript.

Competing interests

The authors declare no competing interests.

Additional information

Supplementary information The online version contains supplementary material available at <https://doi.org/10.1038/s42004-022-00739-8>.

Correspondence and requests for materials should be addressed to Ikutaro Hamada or Takahiro Kondo.

Peer review information *Communications Chemistry* thanks Zhenyu Sun, Pei-Zhou Li, and the other, anonymous, reviewer(s) for their contribution to the peer review of this work.

Reprints and permission information is available at <http://www.nature.com/reprints>

Publisher's note Springer Nature remains neutral with regard to jurisdictional claims in published maps and institutional affiliations.



Open Access This article is licensed under a Creative Commons Attribution 4.0 International License, which permits use, sharing, adaptation, distribution and reproduction in any medium or format, as long as you give appropriate credit to the original author(s) and the source, provide a link to the Creative Commons license, and indicate if changes were made. The images or other third party material in this article are included in the article's Creative Commons license, unless indicated otherwise in a credit line to the material. If material is not included in the article's Creative Commons license and your intended use is not permitted by statutory regulation or exceeds the permitted use, you will need to obtain permission directly from the copyright holder. To view a copy of this license, visit <http://creativecommons.org/licenses/by/4.0/>.

© The Author(s) 2022